



Radiotherapy Hot Paper

How to cite:

International Edition: doi.org/10.1002/anie.202100002

German Edition: doi.org/10.1002/ange.202100002

In Vivo X-ray Triggered Catalysis of H₂ Generation for Cancer Synergistic Gas Radiotherapy

Ying Wu, Lichao Su, Meng Yuan, Tao Chen, Jiamin Ye, Yifan Jiang, Jibin Song,* and Huanghao Yang*

Abstract: To date, hydrogen (H₂) therapy has received widespread attention. However, X-ray triggered sustainable H₂-producing materials with controlled release for cancer treatment have not been reported. Herein, an X-ray triggered sustainable in situ H₂ producing platform, Au NR-TiO₂@ZnS:Cu,Co-A (Au-TiO₂@ZnS), composed of Au-amorphous TiO₂ nano-dumbbell-shaped heterostructure coated with long afterglow particles, was developed for cancer synergistic H₂-radiotherapy. The mechanism of H₂ production was verified by theoretical calculations and in vitro experiments. Changes in the apoptosis pathway caused by the synergistic effect of H₂ and radiotherapy were reported. Guided by its excellent photoacoustic imaging capabilities, mice with orthotopic liver cancer achieved excellent therapeutic effects and low inflammatory side effects, suggesting that Au-TiO₂@ZnS has promising application potential for cancer treatment and prognosis.

Introduction

As a new type of treatment^[1] and one of the signal molecules in the human body,^[2] hydrogen gas (H₂) has shown great application potential as an anti-inflammatory^[3] and anti-cancer agent.^[4] However, the current H₂ therapy systems in clinic involve a systemic supply of low H₂ concentrations, which lack precise release control and targeting capabilities. This greatly limits the efficiency of treatment and the scope of clinical application. After years of development, many nanomaterials are used in the delivery of drugs or as precursor prodrugs for the treatment of diseases in the body, which can potentially be good H₂ carriers or generators as well. At present, some nanomaterials such as palladium,^[5] metal-organic frameworks (MOFs),^[6] and dopamine^[7] have been used to directly carry H₂ or precursors that can produce H₂ in

response to stimulation in the body for the collaborative treatment of cancer. Studies have reported that H₂ can not only cooperate with photothermal therapy to treat cancer, but also can react with malignant free radicals such as peroxy-nitrite and regulating cell pathways and inflammatory factors to treat cancer and anti-inflammatory.^[2,5,8] Nevertheless, more specific mechanisms are still waiting to be reveal. Besides, these nanomaterials usually have a low cargo loading rate and lack the ability to continuously produce H₂. Therefore, preparing a platform that can accurately control the sustained release of H₂ in the body is essential to broaden the application of H₂ therapy in the clinical field.

The photocatalytic H₂ production technology currently used in the energy sector is booming. Nevertheless, most of the materials used for catalyzing H₂ production are in the visible light region for practical purposes.^[9] At the same time, their large size and lack of biocompatibility make them unsuitable for biological applications. As a light source, X-ray irradiation has been widely used in medical imaging^[10] and tumor treatment^[11] owing to its high energy and high penetration depth,^[12] which can be of great significance for photocatalytic H₂ production in vivo but is rarely reported. X-ray excited long afterglow materials are gradually attracting attention in the biomedical field due to their ability to store energy and emit light with time delay.^[13] By making full use of the excess energy of X-rays and releasing afterglow to maintain the photocatalytic process of H₂ after the radiation is stopped, the use of X-ray-excited afterglow materials for catalytic H₂ production in the body has a very promising application potential.

Herein, we designed a dumbbell-shaped gold-TiO₂ hetero-junction structure coated with a long afterglow material (Au-TiO₂@ZnS:Cu,Co-A, abbreviated as Au-TiO₂@ZnS) as a catalytic H₂ production platform for combined H₂ therapy and radiotherapy (Scheme 1). With the photocatalytic ability comparable to anatase,^[14] amorphous TiO₂ does not require high-temperature synthesis conditions, which greatly reduces the difficulty of synthesis. The Au-TiO₂ nano dumbbells (Au-TiO₂ NDs) heterojunction structure can expand the photocatalytic absorption wavelength range of TiO₂.^[15] Moreover, the hot electrons generated by the X-ray excitation effectively promote the separation of electrons and holes in TiO₂, greatly improving the catalytic H₂ production capacity of TiO₂. As the main component of the material, gold nanorods (Au NRs) can enhance radiotherapy sensitivity,^[16] which can provide greater assurance for the synergy of radiotherapy and H₂ therapy. Moreover, the enrichment of the Au NRs material in the lesion area and its metabolism in the body can also be

[*] Y. Wu, L. C. Su, M. Yuan, T. Chen, J. M. Ye, Y. F. Jiang, Prof. J. B. Song, Prof. H. H. Yang

MOE Key Laboratory for Analytical Science of Food Safety and Biology, College of Chemistry, Fuzhou University

Fuzhou 350108 (P. R. China)

E-mail: jibinsong@fzu.edu.cn

hhyang@fzu.edu.cn

Prof. J. B. Song, Prof. H. H. Yang

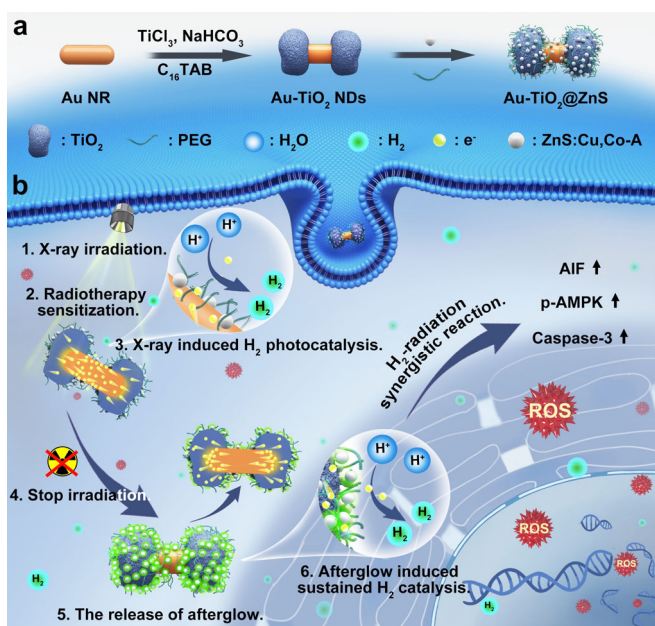
Fujian Science & Technology Innovation Laboratory for

Optoelectronic Information of China

Fuzhou 350108 (P. R. China)

Supporting information and the ORCID identification number(s) for the author(s) of this article can be found under:

<https://doi.org/10.1002/anie.202100002>.



tracked and real-time monitored through photoacoustic imaging.^[17] Finally, the long afterglow material enables Au-TiO₂@ZnS to continue releasing H₂ after stopping X-ray irradiation, which can reduce the side effects of X-rays while further enhancing the H₂ concentration in the lesion area. Both *in vitro* and *in vivo* data demonstrate that Au-TiO₂@ZnS exhibits a good synergistic therapeutic effect of H₂ gas and radiotherapy, and holds promise for development of H₂ therapy.

Results and Discussion

Au-TiO₂ NDs were prepared by bottom-up wet-chemistry method by using C₁₆TAB as a soft template and adjusting the pH through NaHCO₃ to control the degree of hydrolysis of TiCl₃, according to the previous report with some slight modifications.^[15] As the core of Au-TiO₂ NDs growth, Au NRs with a length of about 87 nm and a diameter of 32 nm were synthesized by the classical seed growth method (Supporting Information, Figure S1 a). The amorphous TiO₂ grew on both ends of the Au NRs due to the sparse distribution of C₁₆TAB at the tip of the Au NRs to form a dumbbell-shaped structure with 25 nm thickness (Figure 1 a,

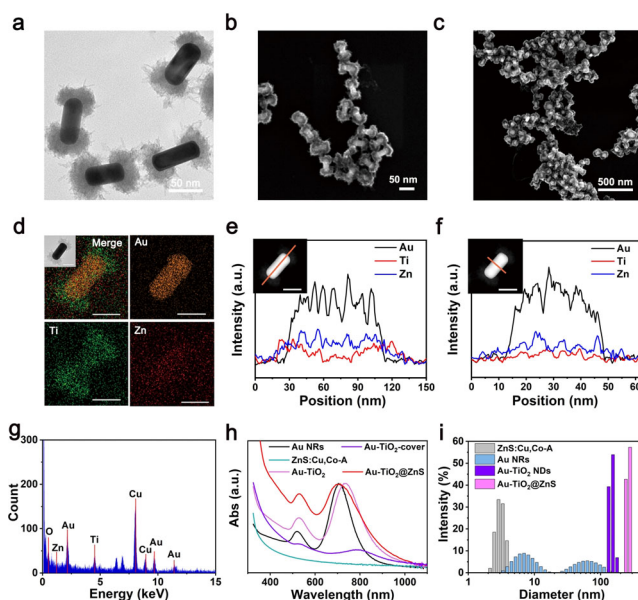


Figure 1. Synthesis and characterization of Au NRs-TiO₂ nano-dumbbells (Au-TiO₂ NDs). a) TEM image, b) SEM images of Au-TiO₂ NDs. c) SEM images of Au-TiO₂@ZnS. d) HAADF-STEM image and elemental maps, and e) transmission electron microscope EDX longitudinal line scan of Au-TiO₂@ZnS (Scale bar, 50 nm). f) Transmission electron microscope EDX horizontal line scan of Au-TiO₂@ZnS (Scale bar, 50 nm). g) EDXS analysis spectrum of Au-TiO₂@ZnS NDs. h) The absorption spectrum of different solutions. i) Size distribution of different samples analyzed by DLS.

b, S1 b). By varying the different reaction parameters, it was found that the concentration of C₁₆TAB and the diameter of the Au NRs played a decisive role in the anisotropic growth of TiO₂. When the concentration of C₁₆TAB was lower or the diameter of Au NRs smaller than 32 nm, it was easier to synthesize the product Au-TiO₂-cover with TiO₂ fully encapsulated (Figure S2). On this basis, increasing the pH of the reaction solution can increase the thickness of the encapsulated TiO₂. ZnS:Cu,Co-A with uniform particle size distribution about 3–5 nm was prepared by adding carboxyl-functionalized adenine (A-COOH) as surfactant and sodium sulfide (Na₂S) reducing precursor solution. The successful carboxyl functionalization of A-COOH was confirmed by ¹H nuclear magnetic resonance (¹H NMR) spectra (Figure S3). The morphology of ZnS:Cu,Co-A was characterized by electron microscopy (Figure S4 a), and its crystal composition was confirmed by X-ray diffraction (XRD), which was consistent with the standard card of ZnS (PDF: 39-1369) (Figure S4 b). Then, ZnS:Cu,Co-A and PEG-SH was bonded on the Au-TiO₂ NDs by electrostatic action and Au-S covalent to obtain Au-TiO₂@ZnS, whose scanning electron microscope (SEM) image was shown in Figure 1 c. From element mapping (Figure 1 d), Transmission electron microscope (TEM) Energy Dispersive X-Ray Spectroscopy (EDX) longitudinal and horizontal line scan (Figure 1 e,f) and Energy Dispersive Spectroscopy (EDS) (Figure 1 g) results of Au-TiO₂@ZnS, it can be observed that the amorphous TiO₂ was mainly distributed at both ends and the long afterglow material was uniformly adsorbed on the surface of Au-TiO₂ NDs. After



that, the light absorption properties of Au NRs, ZnS:Cu,Co-A, Au-TiO₂ NDs, Au-TiO₂-cover and Au-TiO₂@ZnS were measured. It was found that the absorption of nano-dumbbells was mainly distributed in the near-infrared region (NIR), with a maximum absorption peak at 710 nm (Figure 1h). In addition, with the growth of TiO₂, the surface plasmon resonance (LSPR) peak of Au NRs was gradually red shifted. With the formation of heterojunctions, the attachment of afterglow particles and the modified particle size components of PEG-SH became larger, and the average hydrodynamic particle size of Au-TiO₂@ZnS was measured as 210 nm (Figures 1i). The potential of Au-TiO₂@ZnS was more negative than that of Au-TiO₂ NDs, which further indicates the successful modification of ZnS:Cu,Co-A (Figure S5).

It has been reported that under the irradiation of ultraviolet (UV) light, the electrons in TiO₂ in the heterojunction will transfer to Au NRs and undergo a reduction reaction to produce H₂. On the other hand, under the irradiation of visible light, the process of injecting the hot electrons generated by Au NRs into the conduction band of the connected TiO₂ will dominate to catalyze the production of H₂.^[18] Therefore, the macroscopic process of radiotherapy sensitization and photocatalytic H₂ production under X-ray excitation was investigated, as shown in Figure 2a. Under X-ray irradiation, through the injection of tip TiO₂ electrons, the exposed electrons on the side of Au NRs will react with

protons in the water to generate H₂. After stopping the X-ray irradiation, the ZnS:Cu,Co-A that has completed energy storage on the surface of the Au-TiO₂ NDs started to emit the afterglow with main emission light at 578 nm (Figure 2b). The energy loss of Au-TiO₂ NDs photons was negligible because of the extremely small distance between afterglow particles and Au-TiO₂ NDs. This ensured that Au NRs were excited and generated hot electrons, which flowed into TiO₂ where the reduction reaction occurred on its surface. The generated holes in these two processes were captured by the sacrificial agent or OH⁻ and produced by-products and ·OH respectively. These two processes require Au NPs to have exposed parts. For this reason, Au-TiO₂-cover, whose side is completely encapsulated by TiO₂ without exposure, could not achieve catalytic H₂ production.

The afterglow of ZnS:Cu,Co-A lasted for nearly 10 minutes under X-ray (1 Gy, 50 kV, 5 min) irradiation (Figure 2c). Then, the influence of X-ray irradiation and the ability of Au-TiO₂@ZnS to generate H₂ were further explored by using a methylene blue solution containing 2%wt Pt nanoparticles (Figure S6). Considering that the tumor microenvironment is different from normal tissues, glycolytic breathing mainly causes the abnormally increased concentration of lactic acid at the tumor site. Therefore, 5% lactic acid was selected as a sacrificial agent in the in vitro detection of catalytic H₂ production. As seen from the solution

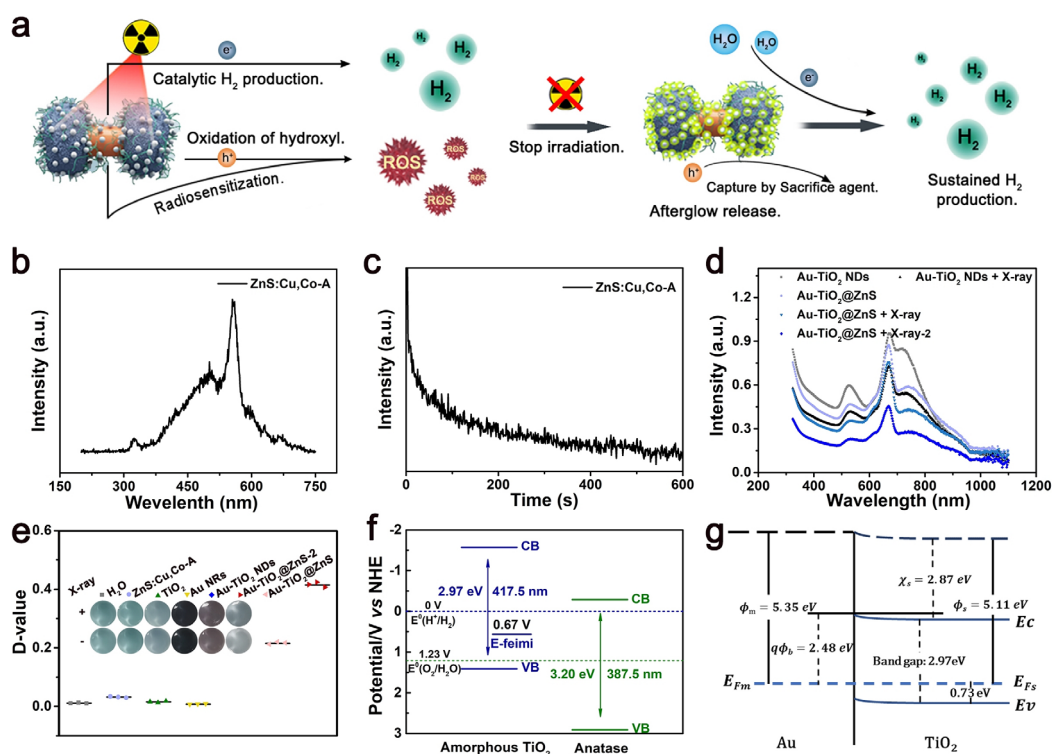


Figure 2. a) Radiosensitization and photocatalytic H₂ production under X-ray excitation. b) The XEOL spectrum and c) The afterglow decay curves of ZnS:Cu,Co-A. d) H₂ production in different solutions was determined by the color change of methylene blue and the absorption change at 665 nm, where the absorption curve of Au-TiO₂@ZnS-2 was measured after stopping X-ray irradiation for 10 min. e) Statistical chart of the difference between 665 nm peaks of different solutions after 5 min of X-ray irradiation. Inset: the corresponding sample picture. f) Representation of the band structures and band gap of the charges in amorphous TiO₂ and anatase in this work, which were calculated according to the theoretical calculation. g) Schottky barrier diagram of contact surfaces of Au NRs and amorphous titania, where Φ_m and Φ_s are the work functions of Au and semiconductor amorphous TiO₂ respectively, χ_s is the electron affinity of TiO₂, and $q\Phi_D$ is the potential barrier.

absorption curve in Figure 2d, after Au-TiO₂ NDs and Au-TiO₂@ZnS were subjected to X-rays (1 Gy, 50 kV, 5 min), the absorption of methylene blue at the maximum absorption wavelength of 665 nm in the solution had significantly decreased for both materials. More importantly, after stopping X-ray irradiation for 10 minutes, the absorption of the Au-TiO₂@ZnS solution at 665 nm showed a further drop (Figure 2e), whereas the absorption curves of the other control groups (Figure S7) did not change further. Meanwhile, gas chromatograph was used to analyze the H₂ generation efficiency of Au NRs, Au-TiO₂-cover, Au-TiO₂ NDs and Au-TiO₂@ZnS. Compared with the H₂ generation efficiency of Au NRs and Au-TiO₂-cover with zero output, that of Au-TiO₂ NDs and Au-TiO₂@ZnS were as high as 101.6 μmol g⁻¹ h⁻¹, 120.2 μmol g⁻¹ h⁻¹, respectively. (Figure S8) This result indicates the significant effect of long afterglow materials on H₂ production after stopping X-ray irradiation.

To further study the mechanism of Au-TiO₂@ZnS catalyzed H₂ generation under X-ray excitation and long afterglow excitation, the conduction band (CB) and valence band (VB) of amorphous TiO₂ were calculated by first-principles and compared with the theoretical values for anatase, which is considered the most active phase for photocatalytic H₂ production. Figure 2f shows that the band gap of amorphous TiO₂ was 2.97 eV, smaller than that of anatase (3.20 eV),^[14] which means that amorphous TiO₂ has a wider spectrum of absorption from ultraviolet light to visible light. In addition, amorphous TiO₂ can more easily lose electrons to catalyze H₂ production, due to its more negative conduction band energy level compared with the H₂ electrode potential ($E^0(\text{H}^+/\text{H}_2)$). Then, the Schottky barrier at the metal-semiconductor interface of Au NRs-TiO₂ was also simulated by first principles (Figure 2g). The contact between Au NRs and amorphous TiO₂ was an ohmic contact because $\Phi_m > \Phi_s$. An anti-blocking layer was produced at the contact interface, which had minimal impact on charge transfer. Moreover, holes flowed from the metal into the semiconductor, forming a hole potential well on the surface of the semiconductor. This is consistent with the direction of electrons flowing from TiO₂ into Au NRs under X-ray irradiation, which slows down the electron-hole recombination efficiency of Au NRs during the H₂ catalytic reduction process to greatly improve the catalytic H₂ production capacity. Under the irradiation of afterglow light in the visible light region, the electron transmission path between Au NRs and amorphous TiO₂ mainly comes from thermionic emission due to SPR, which can cross the Schottky barrier and inject hot electron beams from Au NRs into the conduction band of TiO₂. As a result, reduction and H₂ generation reaction occurs on TiO₂, while leaving holes for oxidation reaction on Au NRs.

The above results verify the ability of X-ray excitation to release H₂ gas and the radio-sensitization effect of Au NRs. Hence, it is worthwhile to conduct in vitro cytotoxicity studies on MC38 cells, which will be used to establish an orthotopic liver cancer model. It can be seen from Figure 3a that in the absence of X-ray radiation, neither ZnS:Cu,Co-A, Au NRs, Au-TiO₂ NDs, nor Au-TiO₂@ZnS exhibited significant toxicity. However, once exposed to X-ray (1 Gy, 50 kV, 5 min),

Au NRs, Au-TiO₂ NDs, and Au-TiO₂@ZnS generally showed significant concentration- and time-dependent cytotoxicity towards cancer cells. Among them, Au-TiO₂@ZnS displayed the most outstanding killing ability.

The mechanism of Au-TiO₂@ZnS's excellent cancer cell killing ability was further explored. It was found that the temperature of the solution changes only 1.9 K after 5 minutes of X-ray (1 Gy, 50 kV) irradiation. The possibility of the fact that local hyperthermia leading to cell death caused by high-energy X-rays interacting with the material could be ruled out (Figure S9). From the results of the Annexin V-PI early apoptosis detection assay, it can be inferred that the exposure of MC38 cells to X-ray (50 kV, 5 min) after 12 h of co-incubation with Au-TiO₂@ZnS mainly led to cell death caused by apoptosis (Figure 3b). The cell cycle results indicated that after X-ray irradiation, the G2-M cycle of MC38 cells was blocked to inhibit cell proliferation (Figure S10). The results of the TUNEL experiment showed that a great number of DNA fragments appeared in the X-ray group, which are represented by bright green FITC fluorescence in Figure 3c, especially in the Au-TiO₂@ZnS co-incubation group. Thus, the primary DNA damage was attributed to the ROS generated during the radiotherapy process. Here, the ROS probe, 2,7-dichlorodihydrofluorescein diacetate (DCFH-DA),^[19] was used to detect the ROS content, which was proportional to the green fluorescence detected in the cells incubated with different materials after X-ray irradiation (Figure 3d). The green fluorescence of the solution corresponding to Au-TiO₂@ZnS under X-ray irradiation was greatly increased compared with that of the control group. This indicates that under the condition of X-ray irradiation and Au-TiO₂@ZnS co-incubation, the cells produced a large amount of ROS. It is well-known that free radicals can cause cell lipid peroxidation damage. Therefore, liposome peroxidation assay was used to verify the degree of lipid peroxidation damage to the MC38 cell membrane after H₂ therapy and radiotherapy. The degree of damage was positively correlated with the measured concentration of MDA. Through the establishment of MDA standard curve (Figures S11, S12). Under X-ray irradiation (1 Gy, 50 kV, 5 min), the lipid peroxidation level of the Au-TiO₂@ZnS group was 5.1 times higher than that of the X-ray group (Figure 3e). The cell proliferation ability after different treatments was also measured through cell cloning experiments. As shown in Figure 3f, S13 the cell cloning rate of the Au-TiO₂@ZnS co-incubation group after X-ray irradiation was almost 0, which was one-thousandth of the control group.

Then, the relative expression of apoptosis inducing factor (AIF), adenosine 5'-monophosphate-activated protein kinase (AMPK) and caspase-3 was characterized by Western blotting to study the effect of the combined action of H₂ and radiotherapy on the apoptosis pathway (Figure 3g). AIF and AMPK related signaling pathways are related factors of non-caspase-dependent apoptosis.^[8b] The levels of AIF decreased after treatment with hydrogen-rich water (HRW) which was prepared by continuously bubbling H₂ with a purity of 99.999% for 5 min by inserting a sterile needle into the culture medium. while AIF levels significantly increased after X-ray irradiation (50 kV, 5 min) in both the groups with or



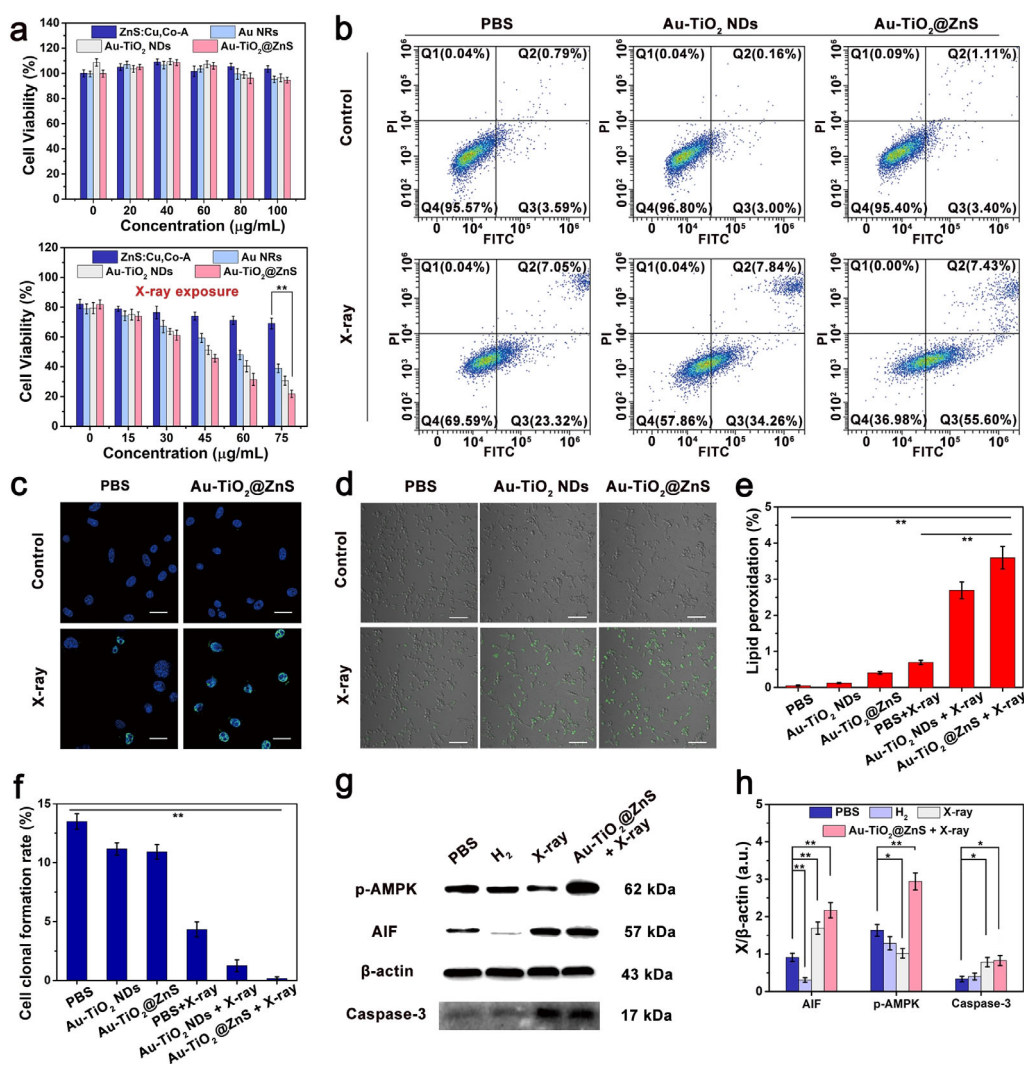


Figure 3. a) Viabilities of MC38 cells treated with PBS, ZnS:Cu,Co-A, Au NRs, Au-TiO₂ NDs and Au-TiO₂@ZnS respectively, with or without X-ray irradiation (1 Gy, 50 kV, 5 min). b) Contour diagram of FITC-Annexin V/PI flow cytometry of MC38 cells after treatment with Au-TiO₂ NDs for 12 h with or without X-ray irradiation (1 Gy, 50 kV, 5 min). (Q1 represents necrotic cells; Q2 shows non-viable late apoptosis/necrosis cells, which are positive for FITC-Annexin V binding and PI uptake; Q3 represents apoptotic cells, FITC-Annexin V positive, and PI negative; Q4 shows viable cells without PI and negative for FITC-Annexin V binding). c) DNA fragmentation and nuclear condensation (scale bar: 25 nm) in MC38 cells with different treatments. d) Confocal fluorescence microscope images of MC38 cells stained by DCFH-DA after different treatments for 12 h with or without X-ray irradiation. Scale bar: 100 μm. e) Lipid damage assessment, measured by lipid peroxidation assays. f) Statistical graph of cell clone formation rate after different treatments. g) Western blot analyses of AIF, p-AMPK, and Caspase 3 for cell apoptosis in MC38-luc cells after treatment with PBS, hydrogen-rich water, X-ray (1 Gy, 50 kV, 5 min) and X-ray (1 Gy, 50 kV, 5 min) in combination with Au-TiO₂@ZnS. h) The relative expression statistics chart was relative to the internal control β-actin. Statistical significance was set to $p < 0.05$ (*) and $p < 0.01$ (**).

without Au-TiO₂@ZnS co-incubation, which indicates the significant impact of X-ray on AIF expression. Compared with the control group, the expression level of phosphorylation-AMPK (p-AMPK) in the Au-TiO₂@ZnS + X-ray group was greatly increased, which was inferred to be the synergistic effect of H₂ and radiotherapy. Notably, after HRW and X-ray treatment, respectively, both of the expression of caspase-3 was slightly enhanced. This enhancement was more prominent in the experimental group, which further reflects the synergistic effect of H₂ and radiotherapy (Figure 3h).

PA imaging has higher spatial resolution and deeper tissue penetration than traditional optical imaging techniques.^[20] Numerous studies have shown that the Au NRs material is

a good photoacoustic imaging agent.^[21] Hence, it was speculated herein that Au-TiO₂@ZnS would also be an excellent near-infrared photoacoustic imaging agent, considering that Au NRs are one of its main components. The in vitro photoacoustic imaging capabilities of Au-TiO₂@ZnS were first explored (Figure S14). A linear relationship was observed between the photoacoustic signal intensity and concentration of Au-TiO₂@ZnS.

To evaluate the long-term safety for further application in biomedicine, the biocompatibility of Au-TiO₂ NDs and Au-TiO₂@ZnS nanoparticles was first studied through hemolysis experiments. The experimental results showed that Au-TiO₂ NDs and Au-TiO₂@ZnS nanoparticles modified with SH-

Polyethylene glycol-COOH (SH-PEG-COOH) did not cause significant hemolysis even at concentrations as high as $160 \mu\text{g mL}^{-1}$ (Figure S15). Then, an orthotopic liver tumor model was established with the luciferase firefly enzyme fluorescent stable expression cell line MC38-luc. By studying the in vivo photoacoustic imaging behavior of Au-TiO₂@ZnS, it was found that the PA signal in liver orthotopic tumors continued to increase with time, suggesting the continuous accumulation of Au-TiO₂@ZnS in the tumor area. It can also be seen from the Figure that Au-TiO₂@ZnS reached the maximum tumor enrichment concentration at 24 h, and it also opened a gap with the liver enrichment concentration (Figure 4a, b), which provides guidance regarding the duration for subsequent radiotherapy. After intraperitoneal injection of fluorescein into mice, the size and spatial distribution of orthotopic liver cancer can be clearly outlined by small animal fluorescence imaging equipment, which provides three-dimensional guidance for local X-ray irradiation during radiotherapy.

Next, the biodistribution and clearance behaviors of Au-TiO₂@ZnS in the hepatoma in situ mice were also fully evaluated. Inductively coupled plasma mass spectrometry (ICP-MS) was employed to measure the concentration of Au in blood or anatomical organs and tumors at different time points after injection. The blood half-lives of Au-TiO₂ NDs and Au-TiO₂@ZnS were 0.51 h and 0.47 h, respectively (Figure S16). From the biodistribution of Au-TiO₂@ZnS in main tissues and tumor (Figure S17, S18), it can be seen that PEG modification promoted the enrichment of Au-TiO₂@ZnS in the tumor area at 24 h after injection, which reached $11.2 \pm 4.8\%$ of the injection dose per gram ($[\text{Au}] \% \text{ID g}^{-1}$). Moreover, Au-TiO₂@ZnS was almost completely metabolized from the body after 7 days.

Given the low-dose and high-efficiency cell killing ability of Au-TiO₂@ZnS in vitro and the high tumor uptake ability in vivo, the anti-tumor effect of Au-TiO₂@ZnS in MC38 orthotopic liver cancer mice was then evaluated by intravenous injection of Au-TiO₂@ZnS (5 mg kg^{-1}). When the fluorescence intensity of the tumor was higher than 2×10^4 ,

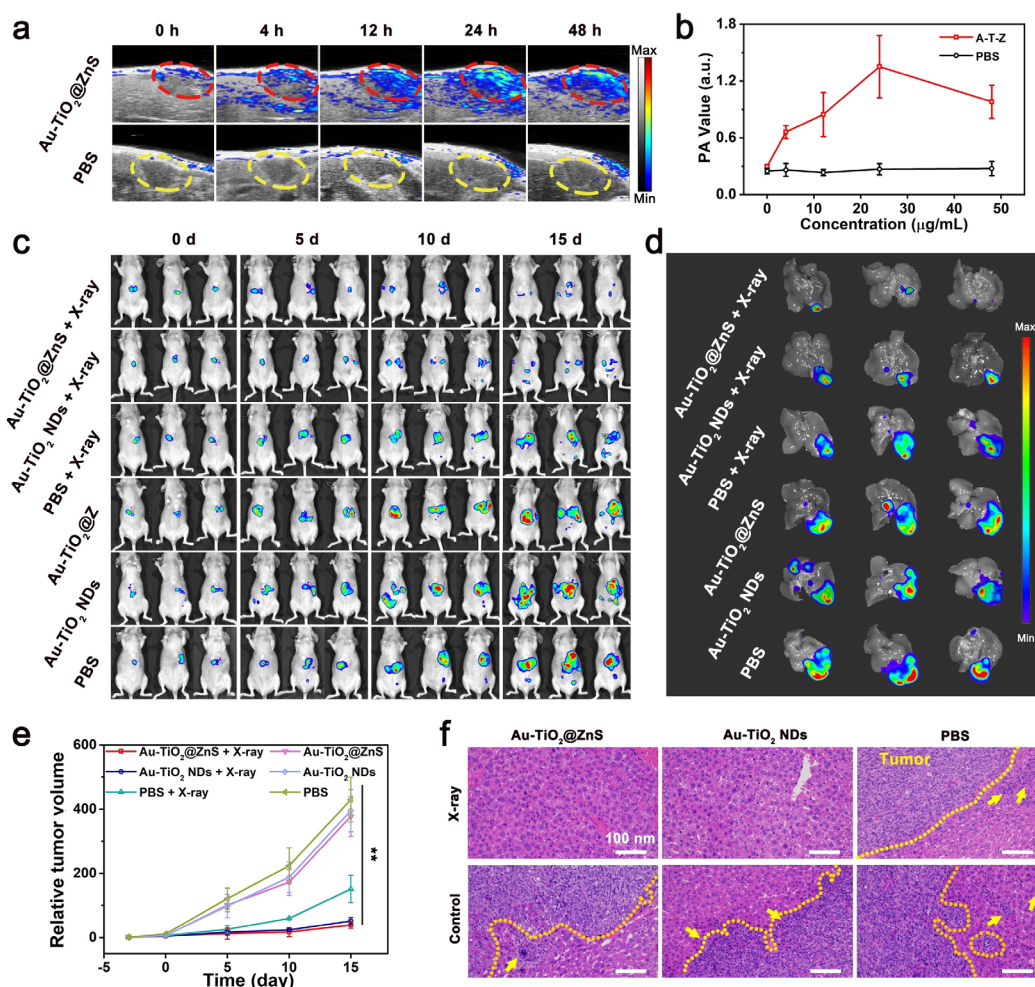


Figure 4. a) Representative PA imaging of mice at 808 nm and b) its corresponding intensity variation curve, taken at different time points after intravenous injection of Au-TiO₂@ZnS and PBS. c) Representative photographs of mice from each group at days 0, 5, 10 and 15 of different treatments. Bioluminescence intensity reflects the volume of tumors. d) A representative photograph of orthotopic liver tumor obtained from each group after 15 days of treatment, where the fluorescence comes from gene-transfected MC38-luc cell lines. e) Tumor volume curves in the different groups. f) H&E staining pictures of representative orthotopic liver cancer sites obtained from sacrificed mice 15 days after different treatments (scale bar: 100 μm).



the mice were divided into the following 6 treatment groups ($n = 5/\text{group}$): (1) PBS, (2) Au-TiO₂ NDs (denoted as Au-TiO₂ NDs), (3) Au-TiO₂@ZnS (4) PBS + X-ray (denoted as X-ray), (5) Au-TiO₂ NDs + X-ray and (6) Au-TiO₂@ZnS + X-ray. The material was injected 24 h in advance and the time for the first radiotherapy (1 Gy, 50 kV, 5 min) was set as the 0th day of treatment. Then, radiation treatments were performed again after 3 days. Figures 4c and d show the representative fluorescence images of orthotopic liver cancer taken on the 0th, 5th, 10th, and 15th days, and the fluorescence images of the intact liver taken out of the sacrificed mice on the 15th day, respectively. The two groups, Au-Ti₂ NDs + X-ray and Au-Ti₂@ZnS + X-ray, displayed obvious tumor growth inhibitory effects. For example, compared with the control group, the tumor suppression rate of the Au-Ti₂@ZnS treatment group was as high as 90.9% on the 15th day of treatment (Figure 4e). The body weight of the mice did not decrease significantly during the entire treatment process (Figure S19). Moreover, the treatment group also significantly improved the survival time of mice (Figure S20).

The blood biochemical indicators of each group of mice, including albumin (ALB), alanine aminotransferase (ALT), aspartate aminotransferase (AST), blood urea nitrogen (BUN), total bilirubin (TBL) and total protein (Tp) were also measured at different time points after injection. No significant changes in these index values were observed between the experimental group and the control group (Figure S21). In addition, the H&E staining of the tissue sections of the main organs of the mice after 15 days of treatment showed that Au-TiO₂@ZnS not only had no obvious toxicity or side effects on each organ, but even reduced the inflammation in the liver because of the inhibition of orthotopic liver cancer and the therapeutic effect of H₂ (Figure S22). As shown in Figure 4f, the tumor site and normal liver cells were separated by a yellow dotted line, in which the cytoplasm was lavender for tumor cells, pink for hepatocytes, and densely distributed dark purple particles representing inflammation are neutrophils. It can be seen that there are no scattered tumor cells and concentrated neutrophils in the liver tissue of the treatment group, indicating that there were almost no metastatic tumor cells in the Au-TiO₂ NDs and Au-TiO₂@ZnS groups, which is in sharp contrast with the obvious tumor aggressiveness in the control group. In the X-ray irradiation-only group, significant white blood cell aggregation was observed around the tumor (shown by the yellow arrow in Figure 4f, indicating the inflammatory side effects of radiotherapy). However, this was not observed in the treatment group, which indicated the good prognostic ability of Au-TiO₂@ZnS tumor treatment. The above results demonstrate that the combined treatment of H₂ and radiotherapy can effectively treat deep-seated tumors and overcome some of the limitations of individual H₂ therapy and radiotherapy in cancer treatment. This work also provides a good demonstration for the precise release and control of H₂ in biochemistry applications.

Conclusion

An X-ray triggered system Au-TiO₂@ZnS was developed for the precise release and control of H₂ in the lesion area for cancer H₂-radiotherapy. The amorphous TiO₂ comprised in Au-TiO₂@ZnS has a lower band gap than anatase, that is, a wider light absorption range. The heterojunction structure of Au-TiO₂@ZnS allows the electrons excited by X-rays to flow smoothly from TiO₂ to Au NRs due to the p-type anti-blocking layer and can generate hot electrons triggered by X-ray excited afterglow luminescence to cross the Schottky barrier. Hence, this heterojunction structure greatly improved the H₂ catalytic reduction efficiency. For the first time, the synergistic effect of H₂ and radiotherapy was reported. The synergistic effect of H₂-radiotherapy not only induces cell death through DNA damage caused by radiotherapy, but also induces cell death by mediating AMPK apoptosis pathway, caspase-3 apoptosis pathway, and expressing AIF to degrade DNA. Taking advantage of the excellent PA imaging ability of Au-TiO₂@ZnS, it was observed that the tumor growth of mice with orthotopic liver cancer was almost completely inhibited. Moreover, the inflammatory side effects caused by radiotherapy were greatly reduced because of the anti-inflammatory effect of the continuous H₂ production excited by afterglow. Therefore, the results indicate that Au-TiO₂@ZnS is a promising H₂-radiotherapy system, which provides a good example for the application of H₂ therapy in cancer treatment and its prognosis.

Acknowledgements

The research was supported by the National Natural Science Foundation of China (Nos. 22027805 and 21874024), National Key R&D Program of China (2020YFA0210800), and the Natural Science Foundation of Fujian Province (No. 2020J02012), and the joint research projects of Health and Education Commission of Fujian Province (No. 2019-WJ-20).

Conflict of interest

The authors declare no conflict of interest.

Keywords: hydrogen gas therapy · long afterglow · photocatalysis · radiotherapy · X-ray

- [1] I. Ohsawa, M. Ishikawa, K. Takahashi, M. Watanabe, K. Nishimaki, K. Yamagata, K. Katsura, Y. Katayama, S. Asoh, S. Ohta, *Nat. Med.* **2007**, *13*, 688–694.
- [2] Y. Wu, M. Yuan, J. Song, X. Chen, H. Yang, *ACS Nano* **2019**, *13*, 8505–8511.
- [3] B. Zhang, F. Wang, H. Zhou, D. Gao, Z. Yuan, C. Wu, X. Zhang, *Angew. Chem. Int. Ed.* **2019**, *58*, 2744–2748; *Angew. Chem.* **2019**, *131*, 2770–2774.
- [4] T. Yang, Z. Jin, Z. Wang, P. Zhao, B. Zhao, M. Fan, L. Chen, T. Wang, B.-L. Su, Q. He, *Appl. Mater. Today* **2018**, *11*, 136–143.
- [5] P. Zhao, Z. Jin, Q. Chen, T. Yang, D. Chen, J. Meng, X. Lu, Z. Gu, Q. He, *Nat. Commun.* **2018**, *9*, 4241.

- [6] G. Zhou, Y. S. Wang, Z. Jin, P. Zhao, H. Zhang, Y. Wen, Q. He, *Nanoscale Horiz.* **2019**, *30*, 1704405.
- [7] C. Zhang, D. W. Zheng, C. X. Li, M. Z. Zou, W. Y. Yu, M. D. Liu, S. Y. Peng, Z. L. Zhong, X. Z. Zhang, *Biomaterials* **2019**, *223*, 119472.
- [8] a) M. Dole, F. R. Wilson, W. P. Fife, *Science* **1975**, *190*, 152–154; b) J. Runtuwene, H. Amitani, M. Amitani, A. Asakawa, K. C. Cheng, A. Inui, *PeerJ* **2015**, *3*, e859.
- [9] a) Y. P. Zhu, J. Yin, E. Abou-Hamad, X. Liu, W. Chen, T. Yao, O. F. Mohammed, H. N. Alshareef, *Adv. Mater.* **2020**, *32*, 1906368; b) J. Yin, F. Zhan, T. Jiao, W. Wang, G. Zhang, J. Jiao, G. Jiang, Q. Zhang, J. Gu, Q. Peng, *Sci. China Mater.* **2020**, *63*, 2228–2238; c) W. Chen, X. Li, F. Wang, S. Javaid, Y. Pang, J. Chen, Z. Yin, S. Wang, Y. Li, G. Jia, *Small* **2020**, *16*, 1902231.
- [10] T. H. Shi, W. J. Sun, R. X. Qin, D. S. Li, Y. S. Feng, L. Chen, G. Liu, X. Y. Chen, H. M. Chen, *Adv. Funct. Mater.* **2021**, *31*, 1903443.
- [11] a) W. Sun, L. Luo, Y. Feng, Y. Qiu, C. Shi, S. Meng, X. Chen, H. Chen, *Adv. Mater.* **2020**, *32*, 2000377; b) H. Deng, L. Lin, S. Wang, G. Yu, Z. Zhou, Y. Liu, G. Niu, J. Song, X. Chen, *Adv. Mater.* **2019**, *31*, 1903443.
- [12] H. Yuan, Y. Zhao, C. Yang, C. Zhang, Y. Yang, H. Meng, S. Huan, G. Song, X. Zhang, *Sci. China Chem.* **2020**, *63*, 924–935.
- [13] a) Y. Lyu, D. Cui, J. Huang, W. Fan, Y. Miao, K. Pu, *Angew. Chem. Int. Ed.* **2019**, *58*, 4983–4987; *Angew. Chem.* **2019**, *131*, 5037–5041; b) Q. Miao, C. Xie, X. Zhen, Y. Lyu, H. Duan, X. Liu, J. V. Jokerst, K. Pu, *Nat. Biotechnol.* **2017**, *35*, 1102–1110.
- [14] C. Gao, T. Wei, Y. Zhang, X. Song, Y. Huan, H. Liu, M. Zhao, J. Yu, X. Chen, *Adv. Mater.* **2019**, *31*, 1806596.
- [15] B. Wu, D. Liu, S. Mubeen, T. T. Chuong, M. Moskovits, G. D. Stucky, *J. Am. Chem. Soc.* **2016**, *138*, 1114–1117.
- [16] a) T.-T. Jia, G. Yang, S.-J. Mo, Z.-Y. Wang, B.-J. Li, W. Ma, Y.-X. Guo, X. Chen, X. Zhao, J.-Q. Liu, S.-Q. Zang, *ACS Nano* **2019**, *13*, 8320–8328; b) Z. He, X. Huang, C. Wang, X. Li, Y. Liu, Z. Zhou, S. Wang, F. Zhang, Z. Wang, O. Jacobson, J. J. Zhu, G. Yu, Y. Dai, X. Chen, *Angew. Chem. Int. Ed.* **2019**, *58*, 8752–8756; *Angew. Chem.* **2019**, *131*, 8844–8848.
- [17] a) K. Pu, *Angew. Chem. Int. Ed.* **2020**, *59*, 7018–7023; *Angew. Chem.* **2020**, *132*, 7084–7089; b) L. Wu, Y. Ishigaki, Y. Hu, K. Sugimoto, W. Zeng, T. Harimoto, Y. Sun, J. He, T. Suzuki, X. Jiang, H. Y. Chen, D. Ye, *Nat. Commun.* **2020**, *11*, 446.
- [18] a) Y. L. Si, S. Cao, Z. J. Wu, Y. L. Ji, Y. Mi, X. C. Wu, X. F. Liu, L. Y. Piao, *Nano Energy* **2017**, *41*, 488–493; b) Y. L. Si, S. Cao, Z. J. Wu, Y. L. Ji, Y. Mi, X. C. Wu, X. F. Liu, L. Y. Piao, *Appl. Catal. B* **2018**, *220*, 471–476.
- [19] Y. Wu, T. Guo, Y. Qiu, Y. Lin, Y. Yao, W. Lian, L. Lin, J. Song, H. Yang, *Chem. Sci.* **2019**, *10*, 7068–7075.
- [20] W. Zhang, J. Wang, L. Su, H. Chen, L. Zhang, L. Lin, X. Chen, J. Song, H. Yang, *Sci. China Chem.* **2020**, *63*, 1315–1322.
- [21] a) Q. Fu, R. Zhu, J. Song, H. Yang, X. Chen, *Adv. Mater.* **2018**, *30*, 1805875; b) S. He, Y. Jiang, J. Li, K. Pu, *Angew. Chem. Int. Ed.* **2020**, *59*, 10633–10638; *Angew. Chem.* **2020**, *132*, 10720–10725; c) J. C. Li, K. Y. Pu, *Acc. Chem. Res.* **2020**, *53*, 752–762.

Manuscript received: January 1, 2021
Revised manuscript received: March 8, 2021
Accepted manuscript online: April 9, 2021
Version of record online: ■ ■ ■ ■ ■ ■ ■ ■ ■ ■

Research Articles

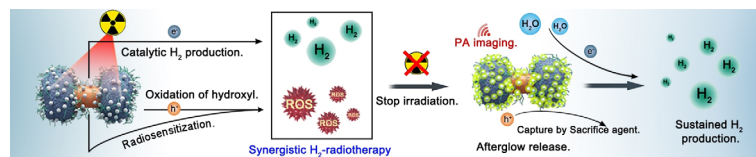


Radiotherapy

Y. Wu, L. C. Su, M. Yuan, T. Chen, J. M. Ye,
Y. F. Jiang, J. B. Song,*
H. H. Yang*



In Vivo X-ray Triggered Catalysis of H₂
Generation for Cancer Synergistic Gas
Radiotherapy



A sustainable in situ H₂ production platform, Au NRs-TiO₂@ZnS:Cu,Co-A (Au-TiO₂@ZnS) was developed for cancer synergistic H₂-radiotherapy triggered by X-rays. The mechanism of hydrogen pro-

duction under X-ray excitation is quite different from that under visible light because of the heterojunction structure of Au NRs-amorphous TiO₂.

